Anomalous anisotropy of the lower critical field and Meissner effect in UTe 2

C. Paulsen, G. Knebel, G. Lapertot, D. Braithwaite, A. Pourret, D. Aoki, F. Hardy, J. Flouquet, J.-P. Brison

Anomalous Anisotropy of the Lower Critical Field and Meissner Effect in UTe_2

C. Paulsen,[1,*] G. Knebel,[2] G. Lapertot,[2] D. Braithwaite,[2] A. Pourret,[2] D. Aoki,[2,3] F. Hardy,[4] J. Flouquet,[2] and J.-P. Brison[2]

[1] *Univ. Grenoble Alpes, Institut Néel, C.N.R.S. BP 166, 38042 Grenoble France*
[2] *Univ. Grenoble Alpes, CEA, Grenoble INP, IRIG, PHELIQS, F-38000 Grenoble, France*
[3] *Institute for Materials Research, Tohoku University, Ibaraki 311-1313, Japan*
[4] *Institute for Solid-State Physics, Karlsruhe Institute of Technology, 76021 Karlsruhe, Germany*

We report on low temperature susceptibility and magnetization measurements made on single crystals of the recently discovered heavy-fermion superconductor UTe_2 and compare the results with the two ambient pressure ferromagnetic superconductors URhGe and UCoGe. Hysteresis curves in the superconducting phase show a familiar diamond shape superimposed on a large paramagnetic background. The Meissner state was measured by zero field cooling in small fields of a few Oe as well as ac susceptibility measurements in small fields and resulted in 100% shielding, with a sharp transition. However the field cooling Meissner-Ochsenfeld effect (expulsion of flux) was negligible in fields greater than just a few Oe, but becomes nearly 30% of the perfect diamagnetic signal when the field was reduced to 0.01 Oe. The critical current due to flux pinning was studied by ac susceptibility techniques. Over the range in fields and temperature of this study, no signature of a ferromagnetic transition could be discerned. The lower critical field H_{c1} has been measured along the three crystalographic axes, and surprisingly, the anisotropy of H_{c1} contradicts that of the upper critical field. We discuss this discrepancy and show that it may provide additional support for a magnetic field-dependent pairing mediated by ferromagnetic fluctuations in UTe_2.

Spin triplet superconductivity (SC) in itinerant ferromagnets close to the ferromagnetic (FM) – paramagnetic (PM) instability was proposed four decades ago [1]. The discovery of the coexistence of ferromagnetism and SC in UGe_2 opened the "rush" to a large variety of experiments [2]. The strong first order nature of the FM – PM transition under pressure at $p_c \approx 1.6$ GPa leads to SC occuring only in the FM domain in the pressure range from 1.2 GPa to 1.6 GPa; the maximum of the superconducting temperature T_c is 0.8 K, but the Curie temperature $T_{Curie} \approx 30$ K.[3]

The field was enriched by the discoveries of two ambient pressure superconducting ferromagnets, URhGe [4] and UCoGe [5], with $T_c = 0.25$ K and 0.8 K, much lower than the respective $T_{Curie} = 9.5$ K and 2.7 K. The rapid suppression of T_{Curie} in UCoGe with pressure leads a the PM ground state above 1 GPa with the persistence of SC far above the critical pressure [6]. For both systems, the weakness of the FM interaction means that transverse magnetic fields (H) applied along the b axis, perpendicular to the easy magnetization axis c, of these orthorhombic crystals gives rise to a spectacular field-enhancement of SC [3, 7, 8].

The recent observation of SC in orthorhombic UTe_2 [9, 10] at $T_c = 1.6$ K opens the possibility to study at ambient pressure spin-triplet SC in a system with a PM ground state located very close to a PM - FM instability. UTe_2 has the highest susceptibility [11] and strong magnetic fluctuations [12] along the a axis. However, the transverse field configuration with $H \parallel b$ attracted the most attention, due to the observation of a strong field-induced reinforcement of SC on approaching the metamagnetic field $H_m \approx 35$ T.[13–16] Most of the published magnetization data in FM SC investigate the field dependence of the FM interaction by longitudinal or transverse field variation. [17–19].

In URhGe and UCoGe the respective FM sublattice magnetization $M_0 = 0.4\ \mu_B$ and $0.07\ \mu_B$ per U-atom produces an internal field of 800 G and 100 G far higher than the estimated value of the lower superconducting critical field H_{c1} of a few gauss. Thus even at $H = 0$, self-induced vortices should occur, as shown for example in the magnetization studies on UCoGe [20].

In this Letter we report low temperature susceptibility and magnetization measurements on two crystals of UTe_2 ($T_c = 1.5$ and 1.6 K). The experiments concentrate on (i) the persistence of the PM state well below T_c K, (ii) the strength of the Meissner effect in field-cooled (FC) experiments, (iii) the proof of a complete superconducting screening in zero field cooled (ZFC) magnetization measurements, (iv) the determination of H_{c1}, and (v) the determination of the London penetration depth and of the the superconducting coherence length from H_{c1} and from the upper critical field H_{c2}. We compare the results with the FM superconductors URhGe and UCoGe.[21]

All the measurements were made using two low-temperature superconducting quantum interference device (SQUID) magnetometers developed at the Institut Néel in Grenoble. A unique feature of the setup is that absolute values of the magnetization can be measured using the extraction method in a field range from 0.01 Oe up to 8 T (for details see the Supplemental Material [21]).

Figure 1 shows hysteresis loops for UTe_2 measured at 100 mK and 1 K below T_c, and at 1.5K in the normal phase for UTe_2 with the field direction along the easy magnetization a axis. The slope of the initial magneti-

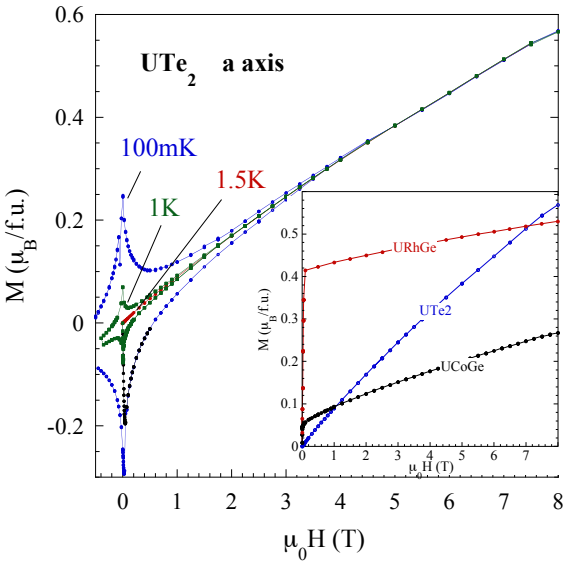

FIG. 1. Magnetization vs field for UTe_2 (sample 1) at 100 mK and 1 K below T_c, and at 1.5 K just above T_c in the normal state with the field along the a axis (easy axis). The insert shows the magnetization of UTe_2 (blue) at 1.5 K, URhGe (red) at 500 mK and UCoGe (black) at 600 mK, i.e. just above their respective T_c in the normal state, with the field along the easy axis.

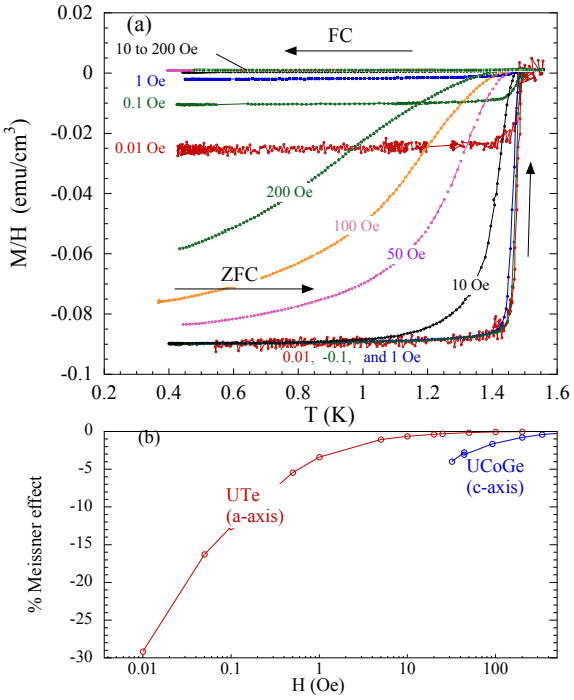

FIG. 2. (a) M/H vs T of UTe_2 (sample 1) for various applied fields ranging from 0.01 to 200 Oe from zero-field-cooled (ZFC) and field-cooled (FC) measurements. (b) The percent Meissner-Ochsenfeld effect (expulsion of flux) plotted against the applied field for UTe_2 (red points) and for UCoGe (blue points). Note that the field range in UCoGe cannot extend below 100mT as the sample needs to be mono-domain. Over the comparable field range, the expulsion of flux is much greater in UCoGe.

zation [also shown later more clearly in Fig. 4(a)] corresponds to 100% shielding. The insert of Fig 1 compares UTe_2 at 1.5K to the two FM superconductors URhGe and UCoGe, with the field applied along their easy c axis, at 500 mK and 600 mK above their respective superconducting states, but far below their respective Curie temperatures. The spontaneous moment of both ferromagnetic superconductors appears clearly, however, it is not a saturated moment: $M(H)$ keeps growing with increasing field. Although there is no spontaneous moment for UTe_2, the PM magnetization increases quickly and becomes larger than in UCoGe at about 1 T, and then greater than in URhGe above 7 T.

The hysteresis loops for UTe_2 have a familiar superconducting diamond shape which is superimposed on a very large PM background response. More hysteresis loops taken close to T_c are shown in Fig. S5 in the Supplemental Material, as well as a comparison with UCoGe in Figs. S6 and S7. In contrast to UCoGe where the superconducting and FM signals are fused together with the FM response dominating [20], our measurements of UTe_2 over the full temperature and field range show that there is no hint of FM behavior down to 80 mK in agreement with muon spin rotation (μSR) experiments.[22]

In Fig. 2(a) the dc susceptibility M/H is plotted against temperature for various applied fields ranging from 0.01 to 200 Oe. Each curve was made by first zero-field-cooling (ZFC) the sample. A dc field was then applied and the sample was slowly warmed above T_c, after which it was re-cooled in the same field, giving the field-cooled (FC) curve. In small dc fields the value of the ZFC susceptibility corresponds to 100% shielding of the field (when demagnetization corrections are made), and the transition is sharp. As the fields are increased, the transition becomes broader and shifts to lower temperatures. The FC susceptibility shows that the Meissner-Ochsenfeld effect (the reversible expulsion of flux as the sample is field-cooled and warmed through T_c) for fields greater than a few Oe is negligible. However for very small fields, the effect becomes more important, reaching about 30% expulsion in a field of 0.01 0e.

We compare this last result to UCoGe along the easy axis in Fig. 2(b). There are important differences. First, the internal fields that are present in UCoGe, of the order 50-100 G, are much greater than H_{c1}, and as a result UCoGe is always in the mixed state, and never achieves 100% shielding. In addition, to measure the Meissner-Ochsenfeld effect in UCoGe means taking into account hysteresis and a coercive field such that the applied field has no meaning while the sample is multi-domain [20]. Nevertheless, a typical value of the percent expulsion of the flux from UCoGe compared to its ef-

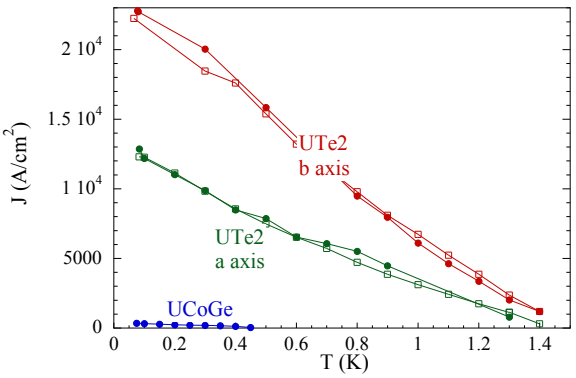

FIG. 3. Current density J_c derived from the critical state model vs temperature for UTe_2 (sample 2) measured along the a and b axes, and for UCoGe along the c axis. The solid round points are data derived from the imaginary part of ac susceptibility, and the open square points are data derived from the remanent magnetization (discussed in the Supplemental Material).

fective shielding would be about 3% expulsion at 50 Oe, which decreases with increasing field. Although small, this is much greater than the Meissner-Ochsenfeld effect observed in UTe_2 in the same field range as can be seen in Fig. 2(b). The other remarkable feature observed in Fig. 2(b) is the non-saturating rate of increase of the Meissner effect down to fields as low as 0.01 Oe in UTe_2: if any internal field exists due to a weak FM phase inside the superconducting phase, the resulting dipolar field has to be much smaller than 0.01 G, or in other words, the ordered moment should be much smaller than $7{\cdot}10^{-6}\ \mu_B$.

A strong hysteresis and a weak Meissner-Ochsenfeld effect suggests strong flux pinning. To confirm this we measured the ac susceptibility χ as a function of the ac driving field: An example can be seen in the Supplemental Material Fig. S20 for the b axis. When flux begins to enter the sample, χ' and χ'' of the ac susceptibility will deviate from their 100% shielding values. The deviations are linear in the applied driving field and the slopes are proportional to $2/(J_c D)$ for χ', and $2/(3\pi J_c D)$ for χ'', where J_c is the current density in the critical state model, and D is the sample width, where we approximate the sample shapes as slabs[23]. The resulting $J_c(H)$ for UTe_2 is plotted in Fig. 3, along with J_c for UCoGe measured along the c axis. Clearly flux pinning is far greater in UTe_2.

The initial magnetization M vs H taken at various constant temperatures is shown in Fig. 4(a). For each curve, the sample was first ZFC. The blue dashed line is a linear fit to the 100 mK data over a field range 0 - 10 Oe The slope of this fit (when corrected for demagnetization effects) corresponds to a susceptibility of $-1/4\pi$ (-1 in SI units) or 100% shielding of the magnetic field. For a given temperature, as the field is increased, the curves deviate from this slope, and this is an indication that flux

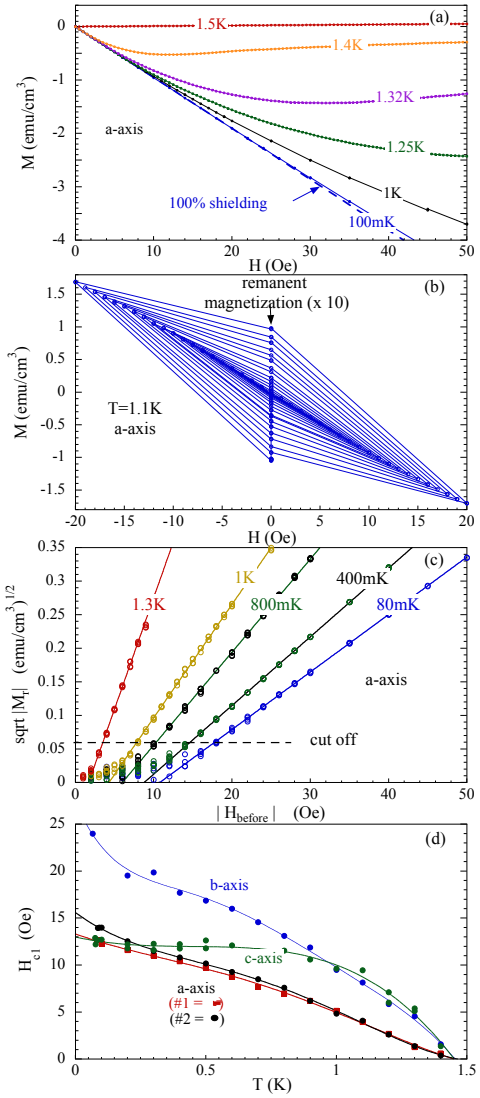

FIG. 4. (a) Initial magnetization M vs H taken a various constant temperatures for UTe_2 (sample 1) with the field along the a axis. The dashed line is a linear fit to the 100 mK data at low fields, and represents 100% shielding. (b) Series of minor hysteresis loops for sample 1 at 1.1 K where the magnitude of the field was systematically increased in steps of 1 Oe, and then returned to zero to measure the point at which a remanent magnetization begins to appear in the sample (the remanent magnetization has been multiplied by 10). (c) The remanent magnetizations is plotted as $\sqrt{M_r}$ vs $H_{\rm before}$ for the a axis for sample 1. The solid lines are linear fits to the data above the cut-off line. (d) $H_{c1}(T)$ for UTe_2 along the a axis for sample 1 (red) and for sample 2 along the a (black), b (blue) and c (green) axis after correcting for demagnetization effects. The lines are guides to the eye.

is entering the sample because H_{c1} has been exceeded. As can be seen in Fig. 4(a), due to the strong pinning, flux enters the sample almost asymptotically and makes the determination of H_{c1} difficult. In addition, because the samples used in this study are not perfect ellipsoids, the

field enters the samples sooner around the edges due to demagnetization effects, further obscuring the real H_{c1}.

A better way to determine H_{c1} is to measure the remanent magnetization as shown in Fig. 4(b) and 4(c) and discussed in detail in the the Supplemental Material. Figure 4(b) is an example of a series of minor hysteresis loops at 1.1 K for sample 1 where the magnitude of the field was systematically increased in small steps, and then returned to zero to measure the point where flux begins to enter the sample. While $H < H_{c1}(T)$ the cycles are reversible. However, when $H_{c1}(T)$ is exceeded, flux begins to enter the sample and the magnetization deviates from the 100% shielding. When the field is then returned to zero, half the flux remains trapped in the sample, and a remanent moment M_r appears. According to the Bean critical state model $M_r \propto H^2_{before}$, i.e. the last field value before the field was reduced to zero and the remanence was measured [24]. In order to estimate H_{c1}, we modify the critical state model following [25] by assuming two regimes: when $H_{before} < H_{c1}$, $M_r = 0$ and when $H_{before} > H_{c1}$, $M_r \propto (H_{before} - H_{c1})^2$.

In Fig. 4(c) we plot an example of the remanent magnetizations for sample 1 as $\sqrt{M_r}$ vs H_{before}. The solid lines are linear fits to the high field data above the cut-off line, thus omitting the low field values where we expect rounding to occur. The intercept gives H_{c1}.

In Fig. 4(d) H_{c1} along the a axis is plotted versus temperature for sample 1, and for sample 2 for the a, b and c axes, where H_{c1} has been corrected for demagnetization effects: Both samples have a platelet shape, with the field applied parallel to the platelet, except for the c axis measurements which was performed perpendicular to the surface. We estimate the value of H_{c1} at $T = 0$ to be 14 Oe along the a and c axis, and 24 Oe along the b axis.

We have also studied H_{c2} along the a axis using bulk ac susceptibility as shown in Fig. S21 of the Supplemental Material and we found $H_{c2}(0) = 5.4$ T along the a axis, in good agreement with published resistivity measurements [9, 10].

However, a comparison of H_{c1} and H_{c2} data reveals a major inconsistency. Indeed, close to T_c in the Ginzburg-Landau (GL) regime, the anisotropy of H_{c1} should be opposite to that of H_{c2} as $H_{c1}H_{c2} = H_c^2(\ln\kappa + 0.49)$, where H_c is the (isotropic) thermodynamic critical field and $\kappa = \frac{\lambda}{\sqrt{2}\xi}$ the anisotropic GL parameter. Hence, neglecting the anisotropy of κ due to the logarithm, with $H^b_{c2} > H^a_{c2} \approx H^c_{c2}$, one expects $H^b_{c1} < H^a_{c1} \approx H^c_{c1}$. In contrast, Fig. 4(c) shows that the relative anisotropies anticipated from H_{c2} are wrong in all directions. Quantitatively, this is a major effect, as the measured H_{c1} anisotropy between a and (b, c) is a factor 3, whereas the H_{c2} anisotropy between (a, c) and b is between 3 and 5, depending on the measurements notably for $H \parallel b$ (see, e.g., Ref. 10). [15, 16]

Such a large discrepancy calls for an explanation. Measurement errors of H_{c1} for $H \parallel b$ might come from stronger pinning in this direction. The critical current has been found indeed twice as large for $H \parallel a$, see Fig. 3(b), but it is very unlikely that it could explain a factor of 10 error between the two directions. The sample geometries are also similar in both cases, excluding an explanation through a bad estimation of the demagnetisation corrections.

So the next step is to question the estimate of H_{c1} from the relations with the GL parameter: for single band s-wave superconductors, these relations hold even in very anisotropic cases (see e.g. [26]). However UTe_2 is most likely p-wave, multigap (like most other heavy-fermion superconductors) and topological [27]. The last feature, implying the existence of low energy surface states might influence pinning, but if it has any influence on the determination of H_{c1}, it should also be reflected in the critical current measurements. More interestingly, the multigap character (or the nodal gap structure [28] for one-dimensional (1D) irreducible representations) has been shown, theoretically (e.g., Ref. 29) and experimentally (e.g., Ref. 30) to induce strong deviations of the anisotropy of the critical fields from the estimations through the GL parameter: But this holds at low temperature, not close to T_c.

Last, several works have reported double transitions in their UTe_2 crystals at zero pressure [31, 32]. Note however that H_{c1} and H_{c2} measurements are only sensitive to the upper transition, until both transition eventually cross under field, which does not happen below 8 T according to Ref. [32]. Hence, whatever the origin of this double transition (intrinsic or due to inhomogeneities), it cannot help to understand the reported anomalous relative anisotropies of H_{c1} and H_{c2}.

A possible explanation for the puzzling anisotropy of H_{c1}, which cannot be completely ruled out, is a low-field change of slope of H_{c2}. This is suggested for example by specific heat measurements [33], which find a weak anisotropy between a and b axis due to a strong curvature of H_{c2} along a (hence a much larger slope at low fields), but still a smaller slope along the c axis. This may partially help to reduce the discrepancy between a and b anisotropies of H_{c1} and H_{c2}, but is still not enough to explain the H_{c1} result, requiring $H^a_{c2} \gg H^b_{c2} \sim H^c_{c2}$.

A key to understanding this anomalous anisotropy might be to take into account that the pairing mechanism in UTe_2 can be tuned by a magnetic field [9, 15], a mechanism inducing a change of slopes of H_{c2} [18, 19], which is not taken into account by GL. A field-dependent pairing induces a field dependence of the "bare" critical temperature $T_c(H)$ that is independent of the mixed state formation, as well as of the Fermi velocities (v_F)[19]. Hence, with field-dependent pairing, both critical fields are functions of field (through T_c and v_F) and temperature and it is easy to show that the measured slope at T_{sc}

is: $\frac{dH_{ci}}{dT} = \frac{\left(\frac{\partial H_{ci}}{\partial T}\right)_H}{1+\frac{dT_{sc}}{dH}\left(\frac{\partial H_{ci}}{\partial T}\right)_H}$. Here, $\left(\frac{\partial H_{ci}}{\partial T}\right)_H$ is the "usual" slope defined for field-independent pairing, for which GL relations should hold. This relation between the measured $\frac{dH_{ci}}{dT}$ and $\frac{\partial H_{ci}}{\partial T}$ shows that, because H_{c1} is three to four orders of magnitudes smaller than H_{c2}, corrections due to $\frac{dT_{sc}}{dH}$ should be negligible on H_{c1}, which should reflect the true bare anisotropies. A $\frac{dT_{sc}}{dH} \approx -0.1$ T/K for $H \parallel a$ and +0.1 T/K for $H \parallel b$, (assuming $\frac{dT_{sc}}{dH} \approx 0$ for $H \parallel c$) could reconcile the lower and upper critical field measurements (see Supplemental Material for more details [21]).

To summarize, the surprising contradiction between lower and upper critical field anisotropies can be understood as a manifestation of the strong field dependence of the pairing strength in UTe_2, which is strongly suppressed along the easy axis and boosted along the hard b axis. Moreover, this is an indication that pairing is suppressed by field along the easy axis in this system, an effect comparable to, although weaker than in UCoGe [18, 19], which can be seen as additional support for ferromagnetic fluctuations mediated pairing.

Moreover, from our very low-field measurements of the Meissner state, we can put an upper limit to any FM ordered moment above 100 mK of 7×10^{-6} μ_B in UTe_2. Restricted Meissner-Ochsenfeld expulsion is coherent with the observed strong pinning. A possible link between the present strong pinning and singular topological properties of the superconducting phase deserve to be clarified.

We thank K. Behnia and T. Klein for fruitful discussions. We acknowledge the financial support of the Cross-Disciplinary Program on Instrumentation and Detection of CEA, the French Alternative Energies and Atomic Energy Commission, and KAKENHI (JP15H05882, JP15H05884, JP15K21732, JP16H04006, JP15H05745, JP19H00646).

* carley.paulsen@neel.cnrs.fr

[1] D. Fay and J. Appel, Phys. Rev. B **22**, 3173 (1980).
[2] S. S. Saxena, P. Agarwal, K. Ahilan, F. M. Grosche, R. K. W. Haselwimmer, M. J. Steiner, E. Pugh, I. R. Walker, S. R. Julian, P. Monthoux, G. G. Lonzarich, A. Huxley, I. Sheikin, D. Braithwaite, and J. Flouquet, Nature **406**, 587 (2000).
[3] D. Aoki, K. Ishida, and J. Flouquet, J. Phys. Soc. Jpn. **88**, 022001 (2019), https://doi.org/10.7566/JPSJ.88.022001.
[4] D. Aoki, A. D. Huxley, E. Ressouche, D. Braithwaite, J. Flouquet, J. Brison, E. Lhotel, and C. Paulsen, Nature **413**, 613 (2001).
[5] N. T. Huy, A. Gasparini, D. E. de Nijs, Y. Huang, J. C. P. Klaasse, T. Gortenmulder, A. de Visser, A. Hamann, T. Görlach, and H. v. Löhneysen, Phys. Rev. Lett. **99**, 067006 (2007).
[6] G. Bastien, D. Braithwaite, D. Aoki, G. Knebel, and J. Flouquet, Phys. Rev. B **94**, 125110 (2016).
[7] F. Lévy, I. Sheikin, B. Grenier, and A. D. Huxley, Science **309**, 1343 (2005).
[8] D. Aoki, T. D. Matsuda, V. Taufour, E. Hassinger, G. Knebel, and J. Flouquet, J. Phys. Soc. Jpn. **78**, 113709 (2009), http://dx.doi.org/10.1143/JPSJ.78.113709.
[9] S. Ran, C. Eckberg, Q.-P. Ding, Y. Furukawa, T. Metz, S. R. Saha, I.-L. Liu, M. Zic, H. Kim, J. Paglione, and N. P. Butch, Science **365**, 684 (2019).
[10] D. Aoki, A. Nakamura, F. Honda, D. Li, Y. Homma, Y. Shimizu, Y. J. Sato, G. Knebel, J.-P. Brison, A. Pourret, D. Braithwaite, G. Lapertot, Q. Niu, M. Vališka, H. Harima, and J. Flouquet, J. Phys. Soc. Jpn. **88**, 043702 (2019), https://doi.org/10.7566/JPSJ.88.043702.
[11] S. Ikeda, H. Sakai, D. Aoki, Y. Homma, E. Yamamoto, A. Nakamura, Y. Shiokawa, Y. Haga, and Y. Ōnuki, J. Phys. Soc. Jpn. **75**, 116 (2006), https://doi.org/10.1143/JPSJS.75S.116.
[12] Y. Tokunaga, H. Sakai, S. Kambe, T. Hattori, N. Higa, G. Nakamine, S. Kitagawa, K. Ishida, A. Nakamura, Y. Shimizu, Y. Homma, D. Li, F. Honda, and D. Aoki, J. Phys. Soc. Jpn. **88**, 073701 (2019), https://doi.org/10.7566/JPSJ.88.073701.
[13] A. Miyake, Y. Shimizu, Y. J. Sato, D. Li, A. Nakamura, Y. Homma, F. Honda, J. Flouquet, M. Tokunaga, and D. Aoki, J. Phys. Soc. Jpn. **88**, 063706 (2019), https://doi.org/10.7566/JPSJ.88.063706.
[14] W. Knafo, M. Vališka, D. Braithwaite, G. Lapertot, G. Knebel, A. Pourret, J.-P. Brison, J. Flouquet, and D. Aoki, J. Phys. Soc. Jpn. **88**, 063705 (2019), https://doi.org/10.7566/JPSJ.88.063705.
[15] G. Knebel, W. Knafo, A. Pourret, Q. Niu, M. Vališka, D. Braithwaite, G. Lapertot, M. Nardone, A. Zitouni, S. Mishra, I. Sheikin, G. Seyfarth, J.-P. Brison, D. Aoki, and J. Flouquet, J. Phys. Soc. Jpn. **88**, 063707 (2019), https://doi.org/10.7566/JPSJ.88.063707.
[16] S. Ran, I.-L. Liu, Y. S. Eo, D. J. Campbell, P. M. Neves, W. T. Fuhrman, S. R. Saha, C. Eckberg, H. Kim, D. Graf, F. Balakirev, J. Singleton, J. Paglione, and N. P. Butch, Nat. Phys. **15**, 1250 (2019).
[17] F. Hardy, D. Aoki, C. Meingast, P. Schweiss, P. Burger, H. V. Löhneysen, and J. Flouquet, Phys. Rev. B **83**, 3 (2011), arXiv:1012.5097.
[18] S. Nakamura, T. Sakakibara, Y. Shimizu, S. Kittaka, Y. Kono, Y. Haga, J. c. v. Pospíšil, and E. Yamamoto, Phys. Rev. B **96**, 094411 (2017).
[19] B. Wu, G. Bastien, M. Taupin, C. Paulsen, L. Howald, D. Aoki, and J.-P. Brison, Nat. Commun. **8**, 14480 (2017).
[20] C. Paulsen, D. J. Hykel, K. Hasselbach, and D. Aoki, Phys. Rev. Lett. **109**, 237001 (2012).
[21] In the Supplemental Material we (1) report details on the single crystal growth, (2)indicate the determination of the thermodynamic critical field, (3) show additional hysteresis very close to T_c, (4) show different methods to determine the lower critical field H_{c1}, and discuss the anisotropy of H_{c1}. The Supplemental Material includes additional Refs. [34–37].
[22] S. Sundar, S. Gheidi, K. Akintola, A. M. Côté, S. R. Dunsiger, S. Ran, N. P. Butch, S. R. Saha, J. Paglione, and J. E. Sonier, Physical Review B **100**, 140502 (2019), arXiv:1905.06901.
[23] F. Gömöry, Superconductor Science and Technology **10**,

523 (1997).
[24] C. P. Bean, Rev. Mod. Phys. **36**, 31 (1964).
[25] M. Naito, A. Matsuda, K. Kitazawa, S. Kambe, I. Tanaka, and H. Kojima, Phys. Rev. B **41**, 4823 (1990).
[26] E. Morosan, L. Li, N. P. Ong, and R. J. Cava, Phys. Rev. B **75**, 104505 (2007).
[27] L. Jiao, S. Howard, S. Ran, Z. Wang, J. O. Rodriguez, M. Sigrist, Z. Wang, N. P. Butch, and V. Madhavan, Nature **579**, 523 (2020).
[28] V. G. Kogan, R. Prozorov, and A. E. Koshelev, Phys. Rev. B **100**, 014518 (2019).
[29] V. G. Kogan, Phys. Rev. B **66**, 020509 (2002).
[30] J. D. Fletcher, A. Carrington, O. J. Taylor, S. M. Kazakov, and J. Karpinski, Phys. Rev. Lett. **95**, 097005 (2005).
[31] S. M. Thomas, F. B. Santos, M. H. Christensen, T. Asaba, F. Ronning, J. D. Thompson, E. D. Bauer, R. M. Fernandes, G. Fabbris, and P. F. S. Rosa, Science Advances **6** (2020), 10.1126/sciadv.abc8709.
[32] I. M. Hayes, D. S. Wei, T. Metz, J. Zhang, Y. S. Eo, S. Ran, S. R. Saha, J. Collini, N. P. Butch, D. F. Agterberg, A. Kapitulnik, and J. Paglione, "Weyl superconductivity in ute2," (2020), arXiv:2002.02539 [cond-mat.str-el].
[33] S. Kittaka, Y. Shimizu, T. Sakakibara, A. Nakamura, D. Li, Y. Homma, F. Honda, D. Aoki, and K. Machida, Phys. Rev. Research **2**, 032014 (2020).
[34] D. Aoki, T. D. Matsuda, F. Hardy, C. Meingast, V. Taufour, E. Hassinger, I. Sheikin, C. Paulsen, G. Knebel, H. Kotegawa, and J. Flouquet, J. Phys. Soc. Jpn. **80**, SA008 (2011), arXiv:1012.1987.
[35] K. Deguchi, E. Osaki, S. Ban, N. Tamura, Y. Simura, T. Sakakibara, I. Satoh, and N. K. Sato, J. Phys. Soc. Jpn. **79**, 083708 (2010), arXiv:1007.1344.
[36] S. Imajo, Y. Kohama, A. Miyake, C. Dong, M. Tokunaga, J. Flouquet, K. Kindo, and D. Aoki, J. Phys. Soc. Jpn. **88**, 083705 (2019), 1907.03033.
[37] G. Knebel, M. Kimata, M. Vališka, F. Honda, D. Li, D. Braithwaite, G. Lapertot, W. Knafo, A. Pourret, Y. J. Sato, Y. Shimizu, T. Kihara, J.-p. Brison, J. Flouquet, and D. Aoki, J. Phys. Soc. Jpn. **89**, 053707 (2020), arXiv:2003.08728.

Supplemental Material for Anomalous Anisotropy of the Low Temperature Susceptibility and Magnetization measurements of UTe_2

C. Paulsen,[1] G. Knebel,[2] G. Lapertot,[2] D. Braithwaite,[2] A. Pourret,[2] D. Aoki,[2,3] F. Hardy,[4] J. Flouquet,[2] and J.-P. Brison[2]

[1] *Univ. Grenoble Alpes, Institut Néel, C.N.R.S. BP 166, 38042 Grenoble France*
[2] *Univ. Grenoble Alpes, CEA, Grenoble INP, IRIG, PHELIQS, F-38000 Grenoble, France*
[3] *Institute for Materials Research, Tohoku University, Ibaraki 311-1313, Japan*
[4] *Institute for Solid-State Physics, Karlsruhe Institute of Technology, 76021 Karlsruhe, Germany*

In this Supplemental Material we show complementary data to those presented in the main article. Furthermore, we give more details on the analysis of the anisotropies of H_{c1} and H_{c2}.

DETAILS ON THE SAMPLE GROWTH

The samples of UTe_2 were synthesized at the CEA-Pheliqs laboratory using chemical vapor transport. The starting elements were 6N Te and pure depleted Uranium, and the transport agent was Iodine (5mg/cm^3), flowing from the source at 1060° toward cold end at 1000° over a period of 10 days. The high quality of the samples was checked by x-ray Laue patterns and SEM XR microanalysis. Sample 1 was studied along the a axis (easy axis) and had a RRR= 16. Specific heat measurements on this sample show a very sharp superconducting transition at $T_c = 1.5$ K. Sample 2 was measured along the a b and c axis and this sample has a $T_c = 1.6$ K. Details of the sample preparations for URhGe and UCoGe can be found elsewhere.[1]

DETAILS OF THE EXPERIMENTAL SETUPS, SAMPLE SHAPES AND DEMAGNETIZATION CORRECTIONS

The measurements were made using two low temperature SQUID magnetometers developed at the Institut Néel in Grenoble. Both magnetometers are equipped with a miniature dilution refrigerator capable of cooling samples below 80 mK. A unique feature of the setup is that absolute values of the magnetization can be obtained by using the extraction method, without heating the sample. One magnetometer has an 8 T superconducting magnet. The second one has a smaller 0.4 T magnet and is dedicated for low fields. The initial low field environment for the second magnetometer is made by using mu- metal shields outside the dewar to reduce the earth's ambient field to below 10 mG. A superconducting lead shield inside the dewar traps and stabilized this field. An active shield placed just inside the superconducting shield and in series with main solenoid insures that the field is never above a few Gauss near the lead superconducting shield.

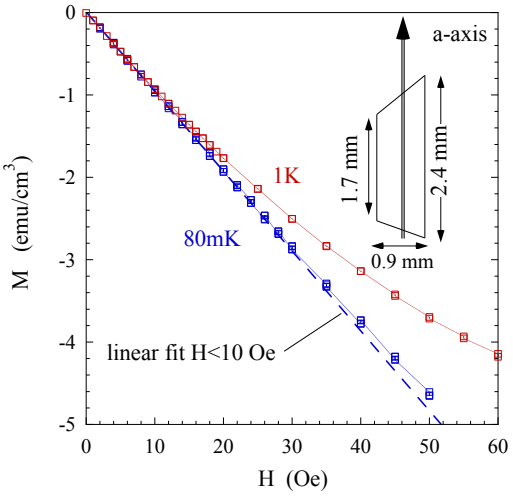

FIG. S1. M vs H along the a axis for sample 1, taken at 80 mK (blue) and 1 K (red). The dashed line is a fit to the 80 mK data for points less than 10 gauss, giving an applied susceptibility $M/H_{\rm applied} = -0.094$ emu/cm^3. The rough shape of sample 1, and the direction of the applied field are shown, the sample thickness was approximately 0.4 mm.

Nevertheless when the applied field becomes greater than 100 Oe or so, flux starts to become trapped in the superconducting wire that makes up the solenoid and in the superconducting flux transformer itself, and this becomes more and more important the larger the field. To minimize these effects, after each field change, the flux transformer is pulse-heated to relieve the flux strain and insure uniform field around the sample. If needed, demagnetizing routines can reduce the trapped flux in the solenoid to below 100 mG.

Notwithstanding, the best strategy for critical low field measurements, as those shown in figure 2 and 4 is simply to plan the experiments at the beginning of a run, and make these measurements first, never increasing the field above 100 Oe.

Figure S1 shows the initial magnetization curve for

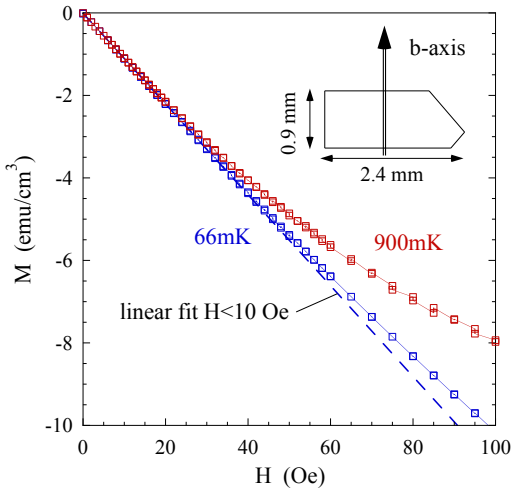

FIG. S2. M vs H along the b axis for sample 2, taken at 66 mK (blue) and 900 mK (red). The dashed line is a fit to the 66 mK data for points less than 10 gauss, giving an applied susceptibility $M/H_{\rm applied} = -0.109$ emu/cm^3. The shape of sample 2 and the field direction are shown in the figure. The sample thickness was approximately 0.3 mm

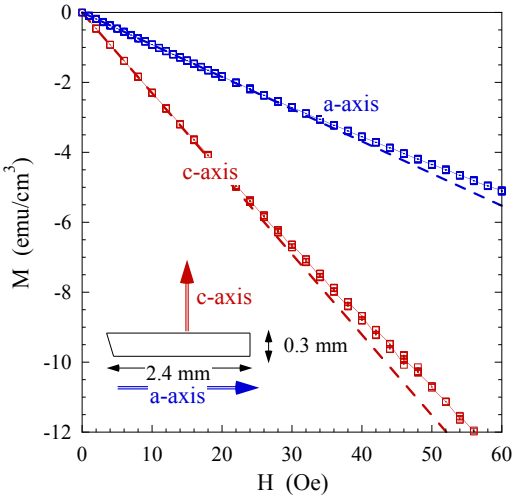

FIG. S3. M vs H along the a axis (blue) and c axis (red) for sample 2, taken at 80 mK. The red dashed line is a fit to data for points less than 4 gauss giving an applied susceptibility $M/H_{\rm applied} = -0.24$ emu/cm^3, the blue dashed line for data for points less than 10 gauss giving an applied susceptibility $M/H_{\rm applied} = -0.09$ emu/cm^3. Sample 2 broke while unglu-ing and the width was reduced to approximately 0.55 mm, the new shape and field directions are shown in the figure.

sample 1 measured at 80 mK and 1 K along the a axis. Figures S2 and S3 show the initial magnetization curves for sample 2 along the a, b and c axis. Both samples had roughly the form of flat platelets as shown in the figures. The mass of sample 1 was 6.88 mg, and the a axis was along the long direction. Sample 2 had a mass of 6.6 mg, and the b axis was along the intermediate direction. Because of the odd shapes, we can only estimate the value of the demagnetization factor using ellipsoids or rectangular shapes. Sample 2 was turned to measure along the a and c axis but unfortunately a portion of the sample broke off. The new mass was 3.9 mg, and the shape of the sample is shown in figure S3 along with the initial magnetization for the two directions.

From the slope of the initial magnetization curves shown in S1 and S2 we find the apparent susceptibility to be - 0.094 and -0.109 emu/cm^3 respectively for the two samples. This would imply effective demagnetization coefficients of $N_{\rm effective}$=2 and 3.5 ($N_{\rm effective}$=0.16 and 0.28 in SI units). The values are on the high side of our rough estimates meaning the applied susceptibility is also on the high side, and implies 100 percent shielding. From figure S3 the initial slope of (the broken) sample 2 along the a and c axis gives apparent susceptibilities of - 0.09 and -0.24 emu/cm^3 respectively. This implies effective demagnetization coefficients of $N_{\rm effective}$=1.4 and 8.4 ($N_{\rm effective}$=0.11 and 0.67 in SI units).

We will use these effective demagnetization values when correcting the data.

DETERMINATION OF THE THERMODYNAMIC CRITICAL FIELD

The specific heat has been measured with a relaxation method down to 100 mK in zero magnetic field on a different sample. The electronic specific heat, shown in Fig. S4a) $C_{\rm el} = C - C_{\rm ph} - C_{\rm div}$ has been determined in the same way than in Ref. 2 by subtracting a phonon contribution ($C_{\rm ph} \propto T^3$) and a small to low temperatures diverging term $C_{\rm div} \propto T^{1-\alpha}$. The dashed line is the expected normal state specific heat taking into account the entropy balance. Figure S4b) shows the temperature dependence of the entropy in the normal and superconducting state. The thermodynamic critical field H_c can be extracted from the difference in the free energy $\Delta F = F_{\rm norm} - F_{\rm sc} = \int_T^{T_c} \Delta S(T) dT = H_c^2/2\mu_0$ of the normal state and the superconducting states. From this analysis we find the isotropic thermodynamic critical field $H_c(0) = 0.0493$ T.

HYSTERESIS LOOPS CLOSE TO THE SUPERCONDUCTING TRANSITION

Figure S5 displays several minor hysteresis loops very close to the superconducting transition T_c for sample 1 with the field applied along the a axis. Clearly, in the superconducting state below T_c the magnetization shows pronounced diamond shape indicating strong pinning on top of a large paramagnetic background. Above T_c only

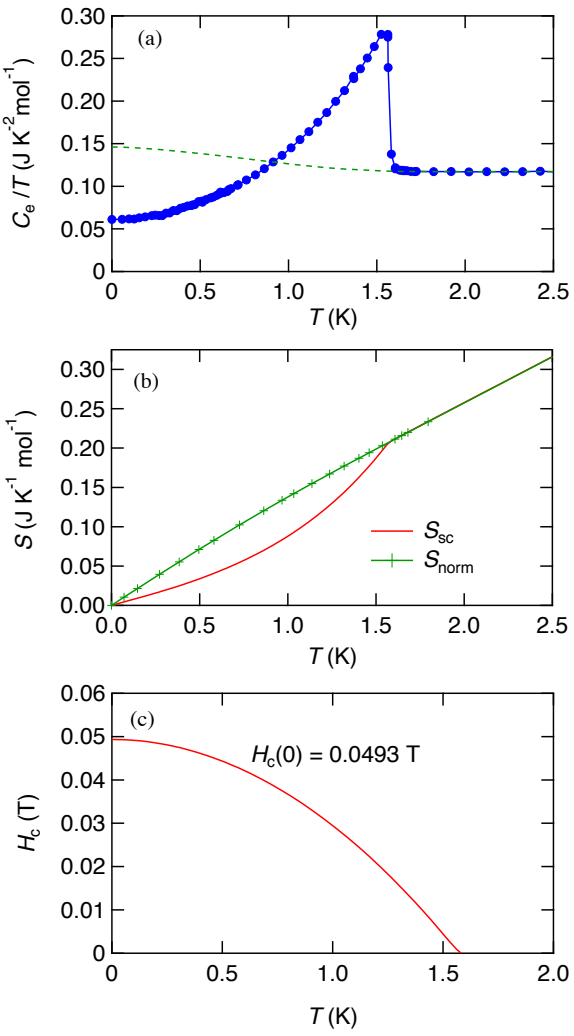

FIG. S4. (a) Electronic specific heat $C_{\rm el}/T$ of UT_2 as function of temperature. $C_{\rm el} = C - C_{\rm ph} - C_{\rm div}$ has been determined following Ref. 2 by subtracting the phonon contribution ($C_{\rm ph} \propto T^3$) The dashed line is the expected specific heat in the normal state taking into account the entropy balance. (b) Temperature dependence of the entropy in the normal (extrapolated below T_c) and superconducting state. (c) Temperature dependence of the thermodynamic critical field H_c deduced from the difference in the free energy $\Delta F = F_{\rm norm} - F_{\rm sc} = \int_T^{T_c} \Delta S(T) dT = H_c^2/2\mu_0$.

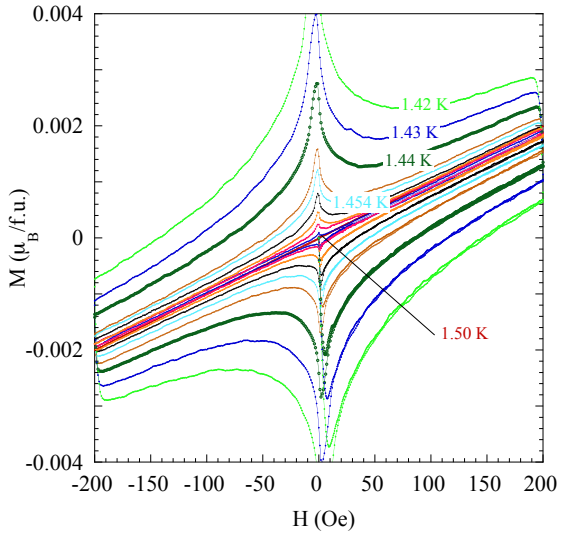

FIG. S5. Series of minor hysteresis loops for UTe_2 with the field direction along the a axis at temperatures close to T_c. The hysteresis loops have a pronounced diamond shape indicating strong pinning. As the temperature approaches T_c, the hysteresis loops collapse onto the relatively large paramagnetic background. No ferromagnetic behavior is observed.

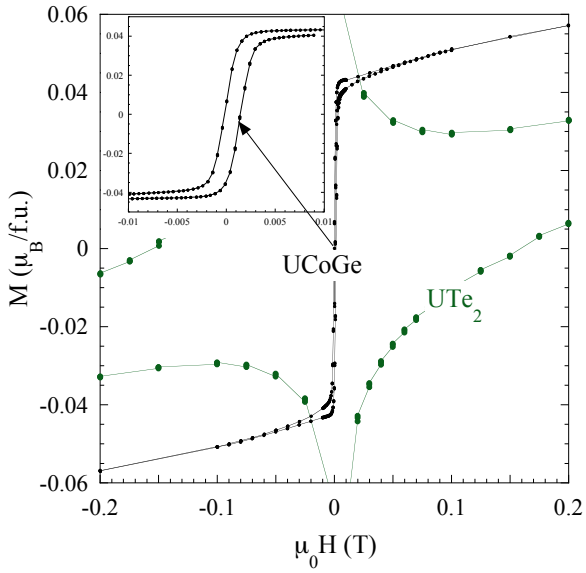

FIG. S6. Hysteresis loops for UTe_2 at 1 K compared with UCoGe at $T = 70$ mK. The pure superconducting hysteresis response of UTe_2 is in contrast to UCoGe where the superconducting and ferromagnetic signals are fused together with the FM response dominating [3]. In fact, at first glance UCoGe does not look superconducting at all. However, the diamond shape response for UCoGe can be revealed by subtracting the hysteresis measured just above the superconducting transition from the low temperature data [4].

the paramagnetic signal is observed. No indication of any ferromagnetic signal is detected.

In Fig. S6 we compare hysteresis loops for UTe_2 at 1 K with that of UCoGe measured at 70 mK. The shape of the hysteresis loops for UCoGe, while in the coexisting ferromagnetic and superconducting state, appears to be dominated by the ferromagnetic response [3]. As shown in Refs. 3 and 4 the characteristic diamond shape of the magnetization of a type-II superconductor can be obtained after the subtraction of the ferromagnetic contribution above the superconducting transition from the

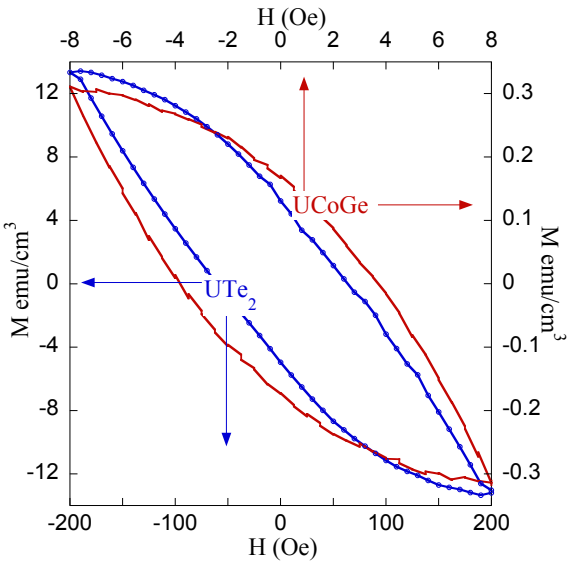

FIG. S7. Minor hysteresis loops for UTe_2 measured at 800 mK, and UCoGe measured at 70 mK. Another way to see the pure superconducting response for UCoGe is to measure minor hysteresis loops using fields smaller than the FM coercive field as shown here. Also shown is a minor loop for UTe_2 but on vastly different scale. The form of these curves can be nicely fitted using the Bean critical state model [5].

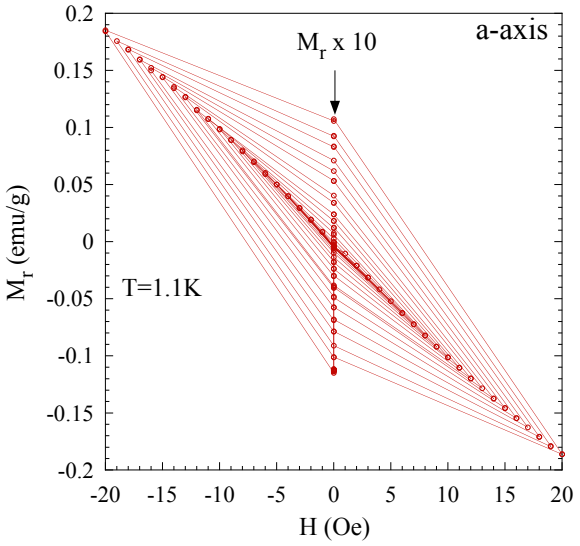

FIG. S8. An example of a series of increasing minor hysteresis loops taken at 1.1 K used for the determination of H_{c1} along the a axis. This data was taken by first zero field cooling the sample to 1.1 K. Then a field of 1 Oe was applied, the magnetization was measured, the field was removed, the magnetization was measured, the field was reversed to -1 Oe, measured, then returned to zero and M_r was measured. The field was then increased to 2 Oe, then back to zero, then to -2 and back to zero and so on, measuring M_r at each field change, and systematically increasing the hysteresis loops by 1 Oe steps up to 20 Oe. While $H < H_{c1}$ the cycles are reversible, and there is no remanent magnetization detected when the field is reduced to zero. However, when H_{c1} is exceeded, then flux begins to enter the sample and the magnetization deviates from the 100% shielding. When the field is returned to zero, one half of the flux is trapped in the sample, and a remanent magnetization appears (in the plot it has been multiplied by 10). The procedure was repeated for different constant temperatures.

low temperature data. This gives clear evidence for the coexistence of superconductivity and ferromagnetism in UCoGe while in UTe_2 no ferromagnetism occurs down to the lowest temperatures. The pure superconducting response for both compounds can be seen in Fig. S7 which shows minor hysteresis loops. This time, for UCoGe, the applied magnetic field was kept smaller than the ferromagnetic coercive field of the sample (~ 10 Oe).

DETERMINATION OF LOWER CRITICAL FIELD H_{c1}

When type-II superconductors have strong pinning, flux enters the sample almost asymptotically, as seen in figures S1, S2 and S3. This makes determination of H_{c1} difficult. In addition, because the samples used in this study were not perfect ellipsoids, the field enters the sample sooner around the edges due to demagnetization effects, further obscuring the real H_{c1}. To overcome this problem, different methods were tried in order to best determine the lower critical field H_{c1}.

The method used for the data shown in Fig. 4d in the main text is based on measurements of the remanent magnetization M_r, and is outlined below and demonstrated in the plots. Using the remanent magnetization when searching for H_{c1} with bulk measurements has advantages. Normally when using the magnetization, one subtracts off the linear part, and the difference is used to observe H_{c1}. At high fields this means that we are subtracting two large numbers in order to extract a small difference. This is not necessary when using the remanent magnetization. In addition the remanent magnetization is measured in zero field, hence with less noise, so that higher SQUID gains can be used. Nevertheless we also show here that using M vs H can give the same result.

An example of the method used to measure the remanent magnetization is shown if figure S8 for sample 1 along the a axis at 1.1 K. The plot shows a sequence of ever increasing hysteresis loops, in steps of 1 Oe, and the resulting remanent magnetization when the field is reduced to zero. Figure S9 shows the results of measurements of the remanent magnetization made at various constant temperatures, plotted in the figure as a function of $H_{\rm before}$, i.e. the last field value before the field was reduced to zero and the remanence was measured.

According to the Bean critical state model (here for

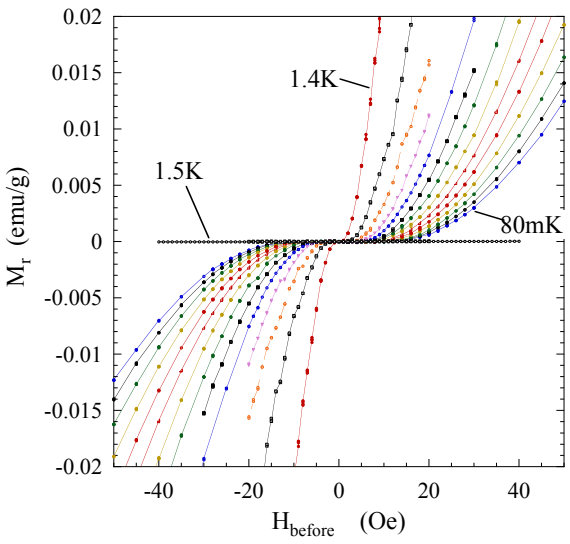

FIG. S9. Remanent magnetization along the a axis measured at various temperatures vs $H_{\rm before}$. The remanent magnetization was measured in zero field as shown in S8, but it is plotted in the figure as a function of $H_{\rm before}$, i.e. the last field value before the field was reduced to zero and the remanence was measured.

a slab-shaped sample), when flux enters a type-II superconductor, the deviation from perfect screening is $\propto H^2$: $-4\pi M = H - H^2/2H^*$ and it retains this flux when the field is removed, giving rise to a remanent magnetization $4\pi M_{\rm r} = H^2_{\rm before}/4H^*$, where $H^* = \pi J_c D/5$ using practical units: H in Oe, D the thickness of the slab in cm, and J_c the critical current i.e the current that impedes the field from penetrating into the sample, in A/cm^2.

In order to make use of these ideas to estimate $H_{\rm c1}$, we assume two regimes above and below $H_{\rm c1}$:

- if $H < H_{\rm c1}$:

$$4\pi M = -H$$
$$4\pi M_{\rm r} = 0$$

- and when $H_{\rm c1} < H < H^*$:

$$4\pi M = -H + (H - H_{\rm c1})^2/2H^*$$
$$4\pi M_{\rm r} = (H_{\rm before} - H_{\rm c1})^2/4H^*$$

We focus on the last equation for $M_{\rm r}$, and ignoring demagnetization corrections for the moment consider three ways to exploit this relation to analyze the data shown in Fig. S9:

1) We can plot the data vs $H^2_{\rm before}$ as shown in Fig. S10, and then fit it to $(H_{\rm before} - H_{\rm c1})^2$.

2) We can plot the data as $M_{\rm r}/H_{\rm before}$ vs $H_{\rm before}$, and fit the data to $(H_{\rm before} - H_{\rm c1})^2/H_{\rm before}$ as shown in figure S11.

3) We plot the data as $\sqrt{M_{\rm r}}$ vs $H_{\rm before}$, and simply fit the data using a linear fit as shown in Fig. S12.

The three fitting procedures give more or less the same result, however fitting the data to $(H_{\rm before} - H_{\rm c1})/H_{\rm before}$ is more robust at lower fields as shown in figure S13.

Figure S14 is an example of data from the second sample measured along the b axis at 66 and 900 mK. The square symbols are the magnetization data minus the linear fit to the data at low field, (i.e. we subtract the dashed line shown in Fig. S2). The circles are the remanent data. The data are plotted as sqrt(M-linear part) and sqrt($|M_{\rm r}|$) vs $H_{\rm before}$. The solid lines are linear fits to the data above the cut off. The figure shows that $H_{\rm c1}$ determined from the magnetization M and from the remanent magnetization $M_{\rm r}$ are equivalent within ± 1 Oe.

An example with demagnetization corrections is shown in Figure S15 for data from the second sample measured along the b axis at 66 mK. The data have been corrected for demagnetization effects using the $N_{\rm effective}$= 3.5 determined from figure S2. The square symbols are the magnetization data minus the linear fit to the data at low field and the circles are the remanent data. The data are plotted as (M-linear part)$/H_{\rm i}$ and $|M_{\rm r}|/H_{\rm i-before}$ vs $H_{\rm i}$ or $H_{\rm i-before}$. Correcting for demagnetization effects gives a critical field about 1.4 times larger along the b axis and about 1.2 times larger along the a axis. The corrected values are used in Fig. 4 of the main text.

The remanent magnetization for sample 2 measured along c axis is shown in Figure S16 , plotted as sqrt($|M_{\rm r}|$) vs $H_{\rm before}$. The dashed lines are fits to the data above the cut-off. Even for measurements perpendicular to the slab, above the cut-off the field still penetrates to a very good approximation as $(H - H_{\rm c1})^2$. However we expect demagnetization corrections to be very important for this

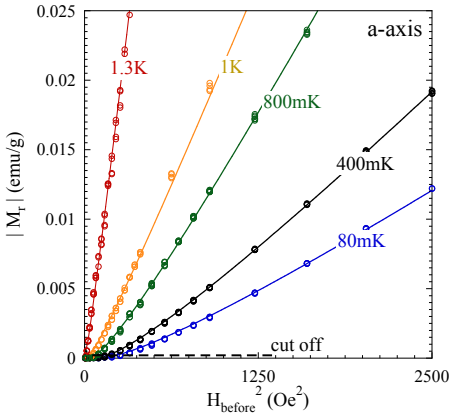

FIG. S10. A few of the curves from figure S9 plotted as $M_{\rm r}$ vs $H^2_{\rm before}$, the square of the last field value before the field was reduced to zero. The solid lines are fits to the data using the form $(H_{\rm before} - H_{\rm c1})^2$. The data below the dashed cut off line were not used in the fits.

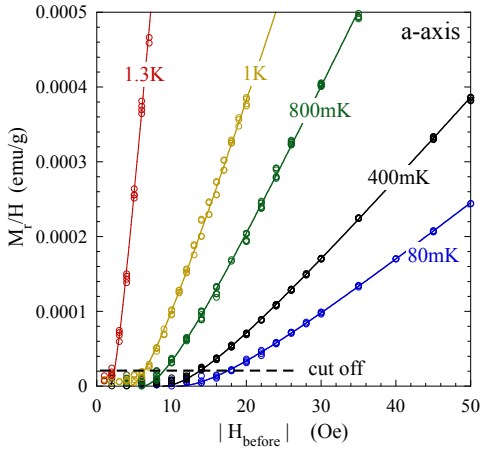

FIG. S11. Example of the same data plotted as remanent M_r/H_{before} vs the absolute value of H_{before}. The solid lines are fits to the data using the form $(H_{before} - H_{c1})^2/H^*$. The data below the dashed cut off line were not used in the fits.

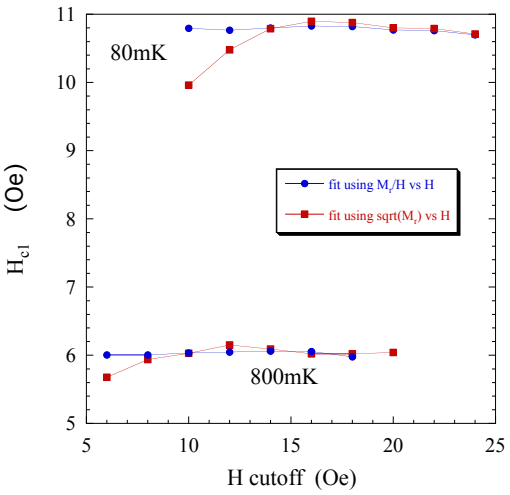

FIG. S13. Example of the sensitivity of fits for H_{c1} vs the cutoff field used for the fits, at 80 mK and 800 mK for the a axis.

direction. To see this we plot M_r for all three directions in Figure S17 as sqrt($|M_r|$) vs H_{before}, i.e. the applied field with out demagnetization corrections, and in Figure S18 as sqrt($|M_r|$) vs $H_{i-before}$, where $H_{i-before}$ is the internal field after correcting for demagnetization effects. As can be seen in the figures, the corrections for the a and b axis are modest, but for the c axis where the field was perpendicular to the slab-shape sample, the corrections are very important, more than doubling the apparent field.

The two parameters used to fit the data are H_{c1} and $1/2H^*$ for the magnetization or H_{c1} and $1/4H^*$ when using M_r. $1/2H^*$ and $1/4H^*$ (roughly the slope of the

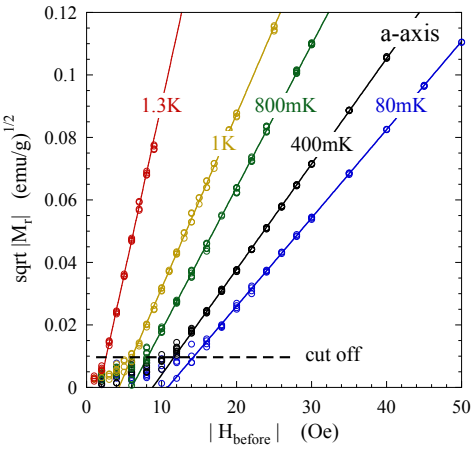

FIG. S12. The data plotted this time as $\sqrt{|M_r|}$ vs absolute value of H_{before}. The solid lines are linear fits to the data above the dashed cut off line. From this figure H_{c1} can be seen as the intersection of the linear fits with the x axis.

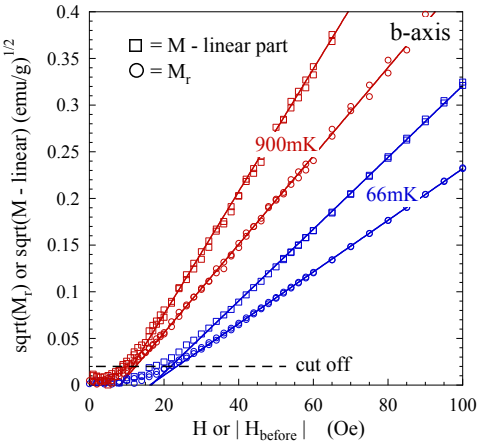

FIG. S14. Plot of the square root of the magnetization minus the linear fit to the data at low field vs H compared to the $\sqrt{|M_r|}$ vs H_{before}. This is data from the second sample measured along the b axis. The solid lines are linear fits to the data above the cut off. The figure shows that H_{c1} determined from the magnetization M or the M_r are equivalent.

points at high field) are inversely proportional to the critical current J_c. From the figure it can be seen that the remanent slope is approximately 1/2 the slope found from the magnetization, as it should in accordance to the critical state model outlined above. Figure S19 shows examples of remanent magnetization for the second sample along the b axis at several temperatures plotted as M_r/H_i vs H_i. In this way we have used the values of the fit of the remanent magnetization to calculate J_c as a function of temperature, and this is reported in figure 4 of the main text along with values obtained from the ac susceptibility.

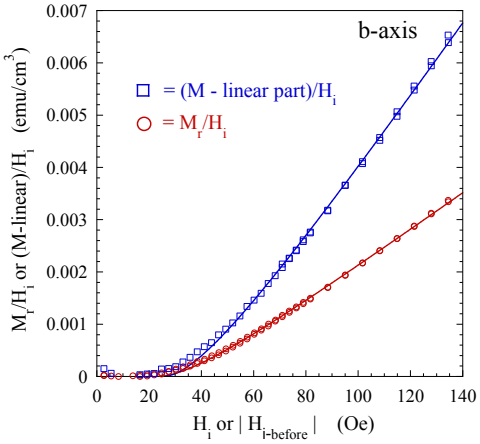

FIG. S15. The same data for the second sample along the b axis at 66 mK as shown in figure S14, but here plotted as $M_{\rm r}/H_{\rm i}$ or $(M - linear)/H_{\rm i}$, vs $H_{\rm i}$, where $H_{\rm i}$ is the internal field after correcting for demagnetization effects. From the figure it can be seen that the remanent slope is approximately 1/2 the slope found from the magnetization, as it should in accordance to the critical state model.

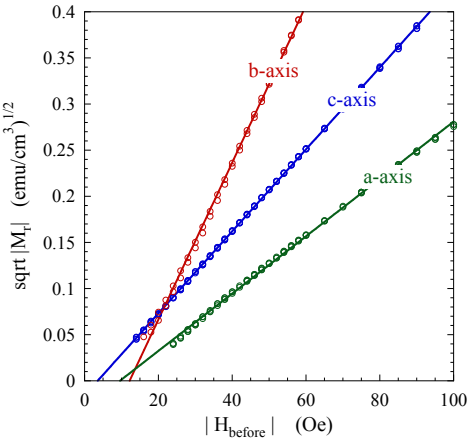

FIG. S17. Sample 2 measured along the a, b and c axis at 300 mK plotted as $\sqrt{|M_{\rm r}|}$ vs $H_{\rm before}$ (the low field points have been cut for clarity). Without demagnetization corrections, a much smaller value of $H_{\rm c1}$ along the c axis would have been obtained.

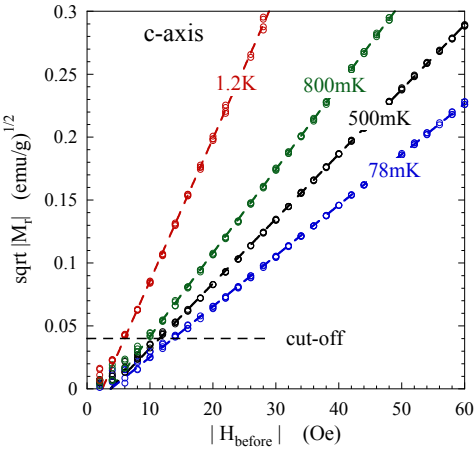

FIG. S16. The remanent magnetization for sample 2 measured along c axis plotted as sqrt($|M_{\rm r}|$) vs $H_{\rm before}$. The dashed lines are fits to the data above the cut-off. Even for measurements perpendicular to the flattest dimension, above the cut-off the field still penetrates to a very good approximation as $(H - H_{\rm c1})^2$.

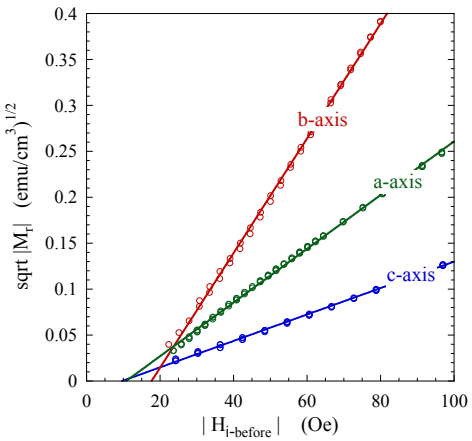

FIG. S18. Same data as shown in figure S16 , but here plotted as sqrt($|M_{\rm r}|$) vs $H_{\rm i-before}$, where $H_{\rm i-before}$ is the internal field after correcting for demagnetization effects. The corrections for the a and b axis are modest, but for the c axis where the field was perpendicular to what was left of the original slab shape, the corrections more than double the apparent field.

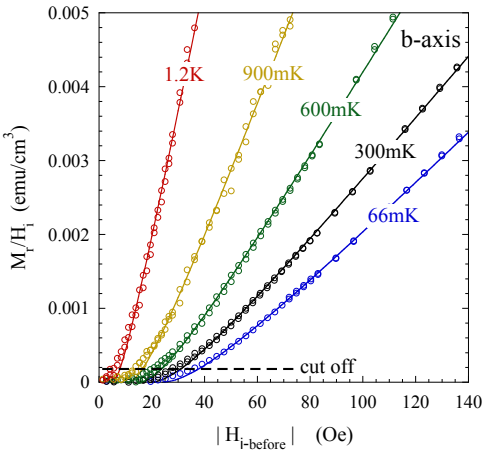

FIG. S19. The remanent magnetization for sample 2, corrected for demagnetization effects at several temperatures plotted as M_r/H_i vs H_i. The solid lines are fits of M_r/H_i against $k(H_i - H_{c1})^2/H_i$, where $k = 1/4H^*$ is inversely proportional to the critical current. Hence the values of the critical current deduced from M_r reported in figure 4 of the main text.

AC SUSCEPTIBILITY χ AND CURRENT DENSITY J_c

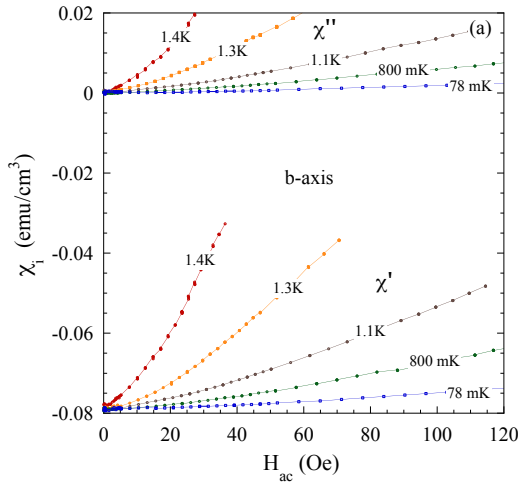

FIG. S20. The real and imaginary parts of the intrinsic ac susceptibility at 1.1 Hz vs the ac driving field H_{ac} for UTe_2 measured along the b axis. The data have been corrected for demagnetization effects. When flux begins to enter the sample, χ' and χ'' of the ac susceptibility will deviate from their 100% shielding values. The deviations are linear in the applied driving field and the slopes are proportional to $2/(J_c D)$ for χ', and $2/(3\pi J_c D)$ for χ'', where J_c is the current density in the critical state model, and D is the sample width where we approximate the sample shapes as slabs.[6]

UPPER CRITICAL FIELD H_{c2}

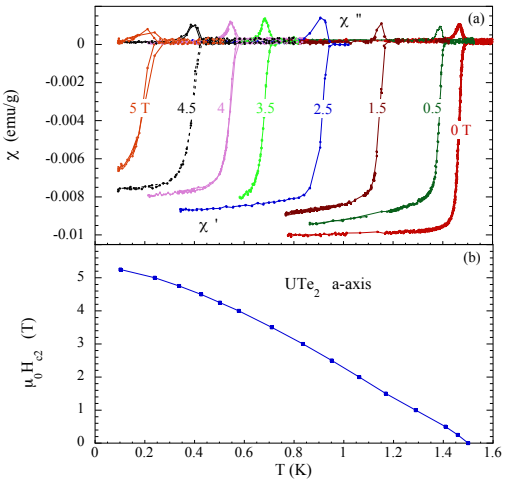

FIG. S21. (a) Real and imaginary parts of the susceptibility vs temperature with various dc fields ranging from 0 to 5 T. The ac driving field was 2 Oe rms at 5.7 Hz. The transition for zero dc field is sharp at 1.5 K, and shifts to lower temperatures as the dc field is increased. Just below the transition a peak in the imaginary part of the susceptibility is observed. (b) The upper critical field H_{c2} defined by the ac susceptibility vs field is shown as a function of temperature.

ANALYSIS OF THE ANISOTROPY OF H_{c1} AND H_{c2}

In the main paper, we explain that a field-dependent pairing can influence the slopes of both H_{c1} and H_{c2} at T_{sc}, and that this change can be expressed from the induced derivative $\frac{dT_{sc}}{dH}$:

$$\frac{dH_{ci}}{dT} = \frac{\left(\frac{\partial H_{ci}}{\partial T}\right)_H}{1 + \frac{dT_{sc}}{dH}\left(\frac{\partial H_{ci}}{\partial T}\right)_H} \quad (1)$$

However, the correction factor in the denominator will be negligibly small for H_{c1}, as it is 3 to 4 orders of magnitude smaller than H_{c2}. Hence, the slope of H_{c1} at T_{sc} is given by the usual expressions, and can be used together with the critical thermodynamic field to estimate, for each crystallographic direction the bare GL parameter κ (see expression 2). From the same GL relations, $\left(\frac{\partial H_{c2}}{\partial T}\right)_H$ can then be obtained.

$$\begin{aligned} H_{c1} &= \frac{H_c}{\sqrt{2}\kappa}\,(ln(\kappa) + 0.49) \\ H_{c2} &= H_c\sqrt{2}\kappa \end{aligned} \quad (2)$$

Knowing $\left(\frac{\partial H_{c2}}{\partial T}\right)_H$, we can invert (1) to obtain the required values of $\frac{dT_{sc}}{dH}$ that could explain the difference

with the measured values of H_{c2}. Table I reports these values. Please note that in table I as well as in Tab. II, the Ginzburg-Landau parameters as well as the coherence length and penetration depth have been deduced from the slopes of the critical fields at T_{sc}, not from their zero-field values. Indeed, even though the Ginzburg-Landau equations are valid only close to T_{sc}, it is more convenient and hence the custom to deduce these values from expressions related to their zero temperature values. This is perfectly fine for single bands weak-coupling superconductors, but may become wrong for multigap, strong coupling unconventional superconductors, which is certainly the case in UTe_2.

TABLE I. The first two lines are experimental data for the slopes of the critical fields at T_{sc}. The slope of the thermodynamic critical field at T_{sc} is $-5.7 \cdot 10^{-2}$ T/K. The GL parameter κ has been deduced from H_{c1} and H_c accordind to (2), and then $\left(\frac{\partial H_{c2}}{\partial T}\right)_H$ (T/K) from these values and the same equations. The required field dependence of the critical temperature, (arising from the field dependent pairing), so as to match $\left(\frac{\partial H_{c2}}{\partial T}\right)_H$ with experimental data for $\left(\frac{dH_{c2}}{dT}\right)$is deduced from (1).

	$H \parallel a$	$H \parallel b$	$H \parallel c$
$\frac{dH_{c1}}{dT}$ (T/K)	$-1.13 \cdot 10^{-3}$	$-3.3 \cdot 10^{-3}$	$-3.8 \cdot 10^{-3}$
$\frac{dH_{c2}}{dT}$ (T/K)	-6.6	-20 / -35	-6.6
κ from H_{c1} & H_c	200	55	45
$\left(\frac{\partial H_{c2}}{\partial T}\right)_H$ (T/K)	-16	-4.4	-3.6
$\frac{dT_{sc}}{dH}$ (K/T)	-0.089	0.2	0.125

However, as explained in the main text, the absolute values of H_{c1} are strongly dependent on the criteria chosen to determine the first flux penetration, and they are probably less reliable than the anisotropy between the different directions. So we also did the same calculation, but renormalizing all H_{c1} values so as to obtain a vanishing $\frac{dT_{sc}}{dH}$ at T_{sc} for $H \parallel c$. Indeed, physically, it is expected that the c axis is more or less "inert", or at least, much less sensitive to field dependent pairing as the easy a axis, where strong suppression might occur like in ferromagnetic superconductors [7, 8], or as the b axis where the metamagnetic transition at $H_m \approx 35$ T induces strong effective mass renormalizations [9, 10]. In order to obtain a vanishing $\frac{dT_{sc}}{dH}$ for $H \parallel c$, we need that $\kappa(H \parallel c)$ matches the value given by the measured H_{c2} in this direction, hence $\kappa(H \parallel c) = 82$. The required correction factor on H_{c1} is 0.63, leading to new values for κ and $\frac{dT_{sc}}{dH}$ reported in table II. We have also put in the table the characteristic length scales of the superconducting state (coherence length ξ_0 and London penetration depth λ_L), deduced from the zero field Fermi velocities and from the GL parameters ($\kappa = \frac{\lambda_L}{\sqrt{2}\xi}$) of table II: we give both these length along each crystallographic direction (ξ_i, λ_i), which depend on the average Fermi velocity in this direction, and for each field direction ($\xi(H \parallel i)$, $\lambda(H \parallel i)$), remembering that the electromagnetic response depends on the average lengths perpendicular to the field. If we want to compare λ_L to published measurements [2] performed at low temperature and for very low fields $H \parallel c$: $\lambda_L \approx 950 - 1200$ nm, then we should use, rather than the slopes, the value of $H^c_{c1}(0)$ and of κ along c, as the temperature dependence of H_{c1} along this direction is very anomalous. From these data, we extract $\lambda_L \approx 1300$ nm, a fairly reasonable agreement.

TABLE II. The first line is experimental data for the slope of H_{c1} at T_{sc}, renormalized by 0.63 so as to obtain no corrections on the slope of H_{c2} for $H \parallel c$ (see text). All other figures where then deduced as explained in the caption of table I.

	$H \parallel a$	$H \parallel b$	$H \parallel c$
$\frac{dH_{c1}}{dT}$ (T/K)	$-0.75 \cdot 10^{-3}$	$-2.1 \cdot 10^{-3}$	$-2.4 \cdot 10^{-3}$
$\frac{dH_{c2}}{dT}$ (T/K)	-6.6	-20 / -35	-6.6
κ from H_{c1} & H_c	336	98	82
$\left(\frac{\partial H_{c2}}{\partial T}\right)_H$ (T/K)	-27	-7.9	-6.6
$\frac{dT_{sc}}{dH}$ (K/T)	-0.11	0.1	0
ξ_i (nm)	14	4.2	3.5
λ_i (nm)	490	1670	2000
$\xi(H \parallel i)$ (nm)	3.85	7.1	7.8
$\lambda(H \parallel i)$ (nm)	1830	990	905

The truth might lie between these two extremes, but in order to discuss "quantitatively" the consequences of this analysis, we chose to focus on the more physical figures of table II. In any case, it is naturally required that the anisotropy of H_{c2}, if it was controlled only by the zero field values of T_{sc} and the Fermi velocities would be opposite to those measured experimentally, with H^b_{c2} slightly smaller than H^c_{c2}, and a very large H^a_{c2} (of order the measured values for H^b_{c2}). This would arise from the field dependent pairing, and using the same model as for the ferromagnetic superconductors [7] and already applied to UTe_2 [11, 12], we can calculate how the strong coupling parameter λ should vary in the three directions in order to reproduce the measured values of H_{c2} reported in [11, 12], starting from the zero field parameters of table II

This is shown on Fig.22, together with previous results on UCoGe and URhGe [7]. Hence, the astonishing conclusion that it is the field dependence of the pairing which reverses the anisotropy of H_{c2} between a and b axis, is less surprising when translated in terms of field dependence of the strong coupling parameter λ: this field dependence, and notably the strong suppression of λ along the easy axis, is similar to what we expect in URhGe and much weaker than what we observe in UCoGe. Only the strong increase of λ for $H \parallel b$ axis is very different in UTe_2, but this is also consistent with the specific heat (C_p) measurements [9, 10], which do show a strong increase of (C_p/T) under field with a finite slope at zero field.

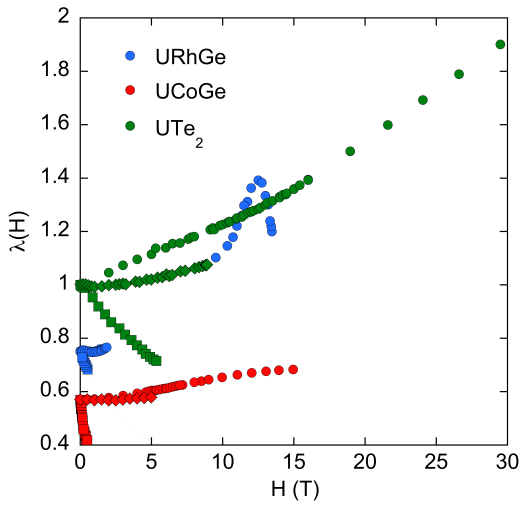

FIG. 22. Comparison of the field dependence of the strong coupling constant λ in the different directions for URhGe (blue), UCoGe (red) as published in [7] and UTe_2 (green) as deduced from H_{c2} data [11, 12] and from the zero field Fermi velocities, yielding the deduced values of $\left(\frac{\partial H_{c2}}{\partial T}\right)_H$ reported in table II. Squares: easy axis, circles: hard axis, diamonds: intermediate axis

[1] D. Aoki, T. D. Matsuda, F. Hardy, C. Meingast, V. Taufour, E. Hassinger, I. Sheikin, C. Paulsen, G. Knebel, H. Kotegawa, and J. Flouquet, J. Phys. Soc. Jpn. **80**, SA008 (2011), 1012.1987.

[2] T. Metz, S. Bae, S. Ran, I.-L. Liu, Y. S. Eo, W. T. Fuhrman, D. F. Agterberg, S. Anlage, N. P. Butch, and J. Paglione, Phys. Rev. B **100**, 220504 (2019).

[3] C. Paulsen, D. J. Hykel, K. Hasselbach, and D. Aoki, Phys. Rev. Lett. **109**, 237001 (2012).

[4] K. Deguchi, E. Osaki, S. Ban, N. Tamura, Y. Simura, T. Sakakibara, I. Satoh, and N. K. Sato, J. Phys. Soc. Jpn. **79**, 083708 (2010), 1007.1344.

[5] C. P. Bean, Rev. Mod. Phys. **36**, 31 (1964).

[6] F. Gömöry, Superconductor Science and Technology **10**, 523 (1997).

[7] B. Wu, G. Bastien, M. Taupin, C. Paulsen, L. Howald, D. Aoki, and J.-P. Brison, Nat. Commun. **8**, 14480 (2017).

[8] S. Nakamura, T. Sakakibara, Y. Shimizu, S. Kittaka, Y. Kono, Y. Haga, J. c. v. Pospíšil, and E. Yamamoto, Phys. Rev. B **96**, 094411 (2017).

[9] A. Miyake, Y. Shimizu, Y. J. Sato, D. Li, A. Nakamura, Y. Homma, F. Honda, J. Flouquet, M. Tokunaga, and D. Aoki, J. Phys. Soc. Jpn. **88**, 063706 (2019).

[10] S. Imajo, Y. Kohama, A. Miyake, C. Dong, M. Tokunaga, J. Flouquet, K. Kindo, and D. Aoki, J. Phys. Soc. Jpn. **88**, 083705 (2019).

[11] G. Knebel, W. Knafo, A. Pourret, Q. Niu, M. Vališka, D. Braithwaite, G. Lapertot, M. Nardone, A. Zitouni, S. Mishra, I. Sheikin, G. Seyfarth, J.-P. Brison, D. Aoki, and J. Flouquet, J. Phys. Soc. Jpn. **88**, 063707 (2019).

[12] G. Knebel, M. Kimata, M. Vališka, F. Honda, D. Li, D. Braithwaite, G. Lapertot, W. Knafo, A. Pourret, Y. J. Sato, Y. Shimizu, T. Kihara, J.-P. Brison, J. Flouquet, and D. Aoki, Journal of the Physical Society of Japan **89**, 053707 (2020).